Temperature Dependence of Optical Bistability in Superconductor–Semiconductor Photonic Crystals Embedded with Graphene

Libing Qian [1,2,†], Yonghong Hu [1,2,†], Zhiyuan Chen [1,2], Dong Zhao [2,3], Junjie Dong [2,*] and Xiaoling Chen [2,3,*]

1   Hubei Key Laboratory of Radiation Chemistry and Functional Materials, Hubei University of Science and Technology, Xianning 437100, China
2   Laboratory of Optoelectronic Information and Intelligent Control, Hubei University of Science and Technology, Xianning 437100, China
3   School of Electronic and Information Engineering, Hubei University of Science and Technology, Xianning 437100, China
*   Correspondence: dongjunjie@hbust.edu.cn (J.D.); xlchen@hbust.edu.cn (X.C.)
†   These authors contributed equally to this work.

Abstract: We theoretically investigate the optical bistability in superconductor–semiconductor photonic crystals composed of graphene. The photonic crystals are symmetric to the center and arranged alternately by the superconductor ($HgBa_2Ca_2Cu_3O_{8+\delta}$) and semiconductor (GaAs) layers. The system supports a defect mode, and graphene is located at the layer interface where the local electric field is the strongest. Consequently, the optical nonlinearity of graphene has been greatly enhanced, and low-threshold optical bistability can be achieved with an incident wavelength red-detuning to the defect mode. The upper and lower thresholds of bistability increase with the increase in the value of low environmental temperature, while the interval between the upper and lower thresholds decreases. This research has a potential application in temperature-controlled optical switches and temperature-controlled optical memory.

Keywords: optical bistability; superconductor; temperature dependence; graphene; photonic crystal

1. Introduction

Optical bistability (OB) is a nonlinear optical phenomenon, in which the single-value input intensity is directly relevant to two different transmission intensities, and the input-output intensity relationship is shown as a hysteresis curve [1–3]. This effect can be applied to multiple components, such as all-optical switches, optical logic devices, optical differential amplifiers, optical diodes, and other elements with extremely fast and controllable function [4–6]. Therefore, optical bistable devices have a promising prospect in all optical communication, optical information processing, and optical computing. In bistability, with the increase in inputting light intensity, the outputting intensity of light jumps upward abruptly at the upper threshold, while with the intensity decrease in incident lights, the output jumps downward at the lower threshold. In other words, the intensity of the incident light triggers the transmitted light to produce a step effect. The incident light intensity at the jump points is called the upper threshold and the lower threshold of OB, respectively. Previous studies have shown that OB can be realized in many structures and materials, such as the nonlinear prism couplers [7,8], semiconductors [9], Fano resonances [10], Fabry–Perot cavities [11], and ring resonators [12]. For optical equipment, it is extremely important to realize the dynamic adjustment of OB. Graphene, as a new two-dimensional material, has both metallic and non-metallic properties. Furthermore, it possesses an ultra-fast and broadband response, low optical loss, and tunability of the surface conductivity [13,14]. Especially, graphene has a strong nonlinear characteristic which can be utilized for OB [15,16] and OB based on photonic crystal (PC) heterostructure/nonlinear graphene as well [17,18].

OB also could be realized based on topological edge states, one-dimensional resonant PCs, the tight-binding model multilayer graphene system, and complex photonic lattices [19–23]. These studies can effectively reduce and tune the threshold of OB. It is a still a challenge, despite the fundamental principle of realizing the OB phenomenon being perfectly clear, so at least the low threshold and simple structure are well planned.

Furthermore, superconducting PCs demonstrate many significative and special electromagnetic properties in striking contrast to the precedent conventional PCs [24–26]. Researchers found that a series of transmission peaks emerge in the major photonic band gap, which is the counterpart of the local modes of light. The bandwidth is particularly susceptible to the thickness of superconductors and environment temperature. Compared with the traditional dielectric PCs, the width of the photonic band gap changes regularly with the change in the width of the whole structure layers. All these characteristics promote the development of photoelectronic devices to be more efficient, such as multiplexers, optical fiber, filter, temperature sensing device, and other applications for optical communication [27]. The superconductor and semiconductor are sensitive to the environment temperature. On the other hand, defect PCs can localize the electric field greatly. Therefore, it is meaningful to combine the superconductor and semiconductor with graphene to form a defect PC and to explore OB and its temperature dependence in this compound system.

Optical bistability is studied in one-dimensional PCs embedded with graphene. The one-dimensional PC is formed by periodic arrangement of superconducting materials and semiconductor materials as well as graphene inlay. The defect modes in the transmission spectrum are presented. Low-threshold tunable OB phenomenon is then illustrated. Furthermore, the relationships between the bistable thresholds, threshold intervals, environment temperature, incident wavelengths, and the chemical potential of graphene are presented. Our work provides a new theoretical approach and inspiration for the study of tunable threshold OB in low-temperature environment and gives a scheme for temperature-controlled non-contact switches.

2. Theoretical Model and Method

Two kinds of medium sheet A and medium sheet B with distinct values in refractive index are arranged to form the one-dimensional PC. The substitution would be: S_1 = ABBA, S_2 = ABABBABA, $\ldots \ldots$, $S_N = (AB)^N (BA)^N$, where N (N = 1, 2, $\ldots \ldots$) is the number of spatial periods of the periodic structure, and N is a positive integer. When N tends to infinity, the structure is one-dimensional PC. When N is finite, the structure is called truncated PC. Two truncated PCs $(AB)^N$ and $(BA)^N$ are combined to form a one-dimensional symmetric structure $(AB)^N (BA)^N$. For example, N = 3, viz. the current structure is ABABABBABABA. Graphene G is embedded into the interface of the medium to form a composite structure $(AB)^{N-1}AGBBGA(BA)^{N-1}$. The schematic of composite structure consisting of superconducting materials, and graphene is shown schematically in Figure 1. The structure is expressed as ABABABBGABABA. The symbol I_i is the incident light, and I_t is the transmitted light. Here, transverse magnetic (TM) polarized light waves are considered to impact the composition and propagate along the Z-axis.
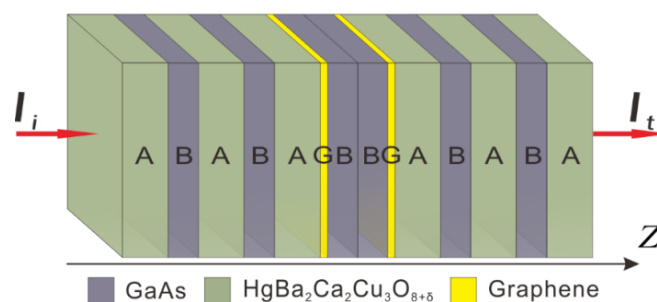

Figure 1. Schematic of composite structure consisting of superconducting materials and graphene. The complex structure can be expressed as ABABAGBBGABABA.

The superconductor and semiconductor component layers can be manufactured by the chemical vapor deposition method which is a common technique in micro- and nano-fabrication. The primary superconducting and semiconducting layers arrange alternatively to satisfy the periodic sequence law. Graphene sheet on a substrate can also be transferred to the interface of two different layers [28], so it is feasible to realize this proposed scheme in experiments completely.

The host materials of medium A and B are $HgBa_2Ca_2Cu_3O_{8+\delta}$ and GaAs, respectively. The superconductor $HgBa_2Ca_2Cu_3O_{8+\delta}$ is a lossless material as environment temperature is below the critical value, and its permittivity is given by

$$\varepsilon_a(\omega) = 1 - \frac{c^2}{\omega^2 \lambda_L^2} \tag{1}$$

where $\omega = 2\pi f$ is the angular frequency of the incident light waves, and $f = c/\lambda$ is the frequency. The London penetration depth λ_L can be expressed as

$$\lambda_L(T) = \frac{\lambda_0}{\left[1 - \left(\frac{T_e}{T_c}\right)^3\right]^{1/3}} \tag{2}$$

where $\lambda_0 = 6.1$ μm, and T_e is the environment temperature. The critical temperature is $T_c = A_1 + B_1 P + D_1 P^2$, $A_1 = 134$, $B_1 = 2.009$, $D_1 = -4.194 \times 10^{-2}$, and the symbol of P represents the hydrostatic pressure applied on the superconductor [29,30].

The superconductor $HgBa_2Ca_2Cu_3O_{8+\delta}$ is anisotropic, and experimental results demonstrate that the maximum London penetration depth are $\lambda_{ab0} = 0.21$ μm and $\lambda_{c0} = 6.1$ μm, respectively [29]. Here in our proposed system, the $HgBa_2Ca_2Cu_3O_{8+\delta}$ layers are local in the ab-plane (or XY-plane) and arrange along the c-axis (or Z-axis); meanwhile, the incident light waves are TM-polarized and normally impinge upon the structure from the left, propagating along the c-axis (or Z-axis). Therefore, the parallel component (along the Z-axis) of permittivity of $HgBa_2Ca_2Cu_3O_{8+\delta}$ which is governed by λ_c determines the optical wave propagating, and the maximum penetration depth is $\lambda_0 = \lambda_{c0}$.

The dielectric constant of the semiconductor material GaAs is

$$\varepsilon_b(P, T_e) = 12.74 e^{-1.73 \times 10^3 P} e^{9.4 \times 10^{-5}(T_e - 75.6)}, T_e < 200\text{K} \tag{3}$$

where K is the absolute temperature unit; P is the hydrostatic pressure [30,31].

The relationship between the thickness of medium sheet B and the pressure is

$$d_b(P) = d_{b0}[1 - (M_{11} + 2M_{12})P] \tag{4}$$

where d_{b0} is the initial thickness of $P = 0$; the elastic constant is $M_{11} = 1.16 \times 10^{-2}$ GPa^{-1}, and $M_{12} = -3.7 \times 10^{-3}$ GPa^{-1} [32,33].

The hydrostatic pressure P on sheet B can make it strain, which is an elastic distortion, with stretching and shrinking in size of the sheet. The layer A also distorts elastically, but elastic constant of material A is one order magnitude lower than the value of material B [33]. Therefore, we neglect the influence of the hydrostatic pressure on the thickness of layer A.

Taking the environment temperature $T_e = 100$ K, $P = 0$ Pa as the standard, the refractive index of $HgBa_2Ca_2Cu_3O_{8+\delta}$ is $n_{a0} = 0.9994$; the refractive index of GaAs is $n_{b0} = 3.5678$, and $\lambda = 1.55$ μm. Based on this, the thickness of medium sheet A and medium sheet B is determined to be 1/4 optical wavelength, respectively; that is, the thickness of A is $d_a = \lambda_0/(4n_{a0}) = 0.3877$ μm. The thickness of B is $d_b = \lambda_0/(4n_{b0}) = 0.1086$ μm.

The surface conductivity of graphene is $\sigma_0(\omega, \mu, \tau, T_e) = \sigma_{intra} + \sigma_{inter}$, which includes the intra-band transition and the inter-band transition of electrons [34]. The first part is defined as

$$\sigma_{intra} = i\frac{e^2 k_B T_e}{\pi \hbar^2(\omega + i\tau^{-1})}\left[\frac{\mu}{k_B T_e} + 2\ln(\exp(-\frac{\mu}{k_B T_e}) + 1)\right] \tag{5}$$

where e, $\hbar$, i, k_B in this equation are, respectively, the electric charge, the Planck constant, the imaginary unit, and the Boltzmann constant. The parameter of τ is the phenomenological relaxation time of electrons, and μ is the chemical potential of graphene. When $\hbar\omega$, $|\mu| \gg K_B T_c$, another part of the graphene conductivity can be represented as

$$\sigma_{\text{inter}} = i\frac{e^2}{4\pi\hbar} \ln\left[\frac{2|\mu| - \hbar(\omega + i\tau^{-1})}{2|\mu| + \hbar(\omega + i\tau^{-1})}\right]. \tag{6}$$

The nonlinear conductivity coefficient of graphene is

$$\sigma_3 = -i\frac{3}{8}\frac{e^2}{\pi\hbar}\left(\frac{eV_F}{\mu\omega}\right)^2\frac{\mu}{\omega} \tag{7}$$

whose Fermi velocity satisfies $V_F \approx c/300$ [35].

The equivalent dielectric constant of graphene is

$$\varepsilon_g = 1 + i\frac{\sigma_0\eta_0}{k_0 d_g} + i\frac{\sigma_3\eta_0}{k_0 d_g}|E_z|^2 \tag{8}$$

Here the equivalent thickness of graphene is set as $d_g = 0.33$ nm, and k_0 represents the wave vector in vacuum. The symbol of $|E_z|^2$ is the local electric field intensity at the position where graphene locates in Z-direction [36,37]. For a normally incident TM-polarized light wave, propagating along with the Z-axis, the magnetic fields contain the orthogonal components H_x and H_y, and the electric field only includes the parallel component E_z. The third order nonlinearity of graphene is proportional to the local electric field intensity of the parallel component $|E_z|^2$.

The one-dimensional photonic crystal layers including graphene arrange along the Z-axis. As light waves normally impinge upon the system from the left and transmit in each layer, one can simulate the linear transmission spectra through the forward transmission matrix method (FTMM) [38,39]. The electromagnetic fields at the incident port of systems are denoted by (E_i, H_i), and at the outputting port it is expressed as (E_o, H_o), of which their relationship is governed by

$$\begin{pmatrix} E_i \\ H_i \end{pmatrix} = M_1 M_2 \cdots M_l \cdots M_{\gamma-1} M_\gamma \begin{pmatrix} E_o \\ H_o \end{pmatrix} = \begin{bmatrix} m_{11} & m_{12} \\ m_{21} & m_{22} \end{bmatrix} \begin{pmatrix} E_o \\ H_o \end{pmatrix} \tag{9}$$

where m_{11}, m_{12}, m_{21}, and m_{22}, respectively, mean the four elements of transfer matrix. The subscript γ represents the total layer number of structures. The transfer matrix of light waves M_i in the ith layer can is given by

$$M_l = \begin{bmatrix} \cos\varphi_l & -\frac{i}{\eta_l}\sin\varphi_l \\ -i\eta_l\sin\varphi_l & \cos\varphi_l \end{bmatrix} \tag{10}$$

For the non-magnetic medium, the transmission phase is $\varphi_1 = 2\pi d_1(\varepsilon_1 - \sin^2\theta)/\lambda$, where θ is the incident angle, and ε_1, d_1, and λ are the permittivity, dielectric thickness, and the wavelength of the incident light, respectively. For a TM-polarized light wave, the light resistivity in each layer is given by $\eta_1 = \varepsilon_1(\varepsilon_0/\mu_0)^{1/2}/(\varepsilon_l - \sin^2\theta)^{1/2}$.

The photonic crystal is placed in free space, and the transmission coefficients can be derived by the expression

$$t = \frac{2\eta_0}{(m_{11} + m_{12}\eta_o)\eta_i + (m_{21} + m_{22}\eta_i)} \tag{11}$$

where the vacuum resistivity for the incident, and outputting ports are $\eta_o = \eta_i = \eta_0 = (\varepsilon_0\mu_0)^{1/2}$, respectively. The transmittance of light waves is derived by $\alpha_T = tt^*$.

The distribution of electric field and the optical bistability are simulated by the inverse transfer matrix method (ITMM) [40]. We view graphene as an equivalent dielectric and denote it by the *l*th layer. The transfer matrix of graphene contains the permittivity item $\varepsilon_l = \varepsilon_g + 1 + i\sigma_0\eta_0/k_0d_g + i\sigma_3\eta_0|E_{z,l}|^2/k_0d_g$. It needs to give a nonlinear correction for the linear permittivity of graphene as a strong laser impinges upon this structure, especially in the process of simulating the optical bistability. We, respectively, set E_o and $H_o = E_o/\eta_0$ as the electric field and the magnetic field at the outputting port. The total transfer matrix of the partial structure from the *l*+1th layer to the last layer is given by $[m'_{11}, m'_{12}; m'_{21}, m'_{22}]$, and the corresponding transmittance of light waves is denoted by α'_T. Then, the electric field at the incident port of the *l*+1th layer is derived by $|E_{z,l}|^2 = |E_o|^2/\alpha'_T$. The electric field distribution can also be calculated by dividing the superconductor and semiconductor layers into a series of slices in nm magnitude, ignoring the nonlinear correction term.

3. Results and Discussion

Figure 2a gives the transmission spectra for $N = 3$, $\mu = 0.5$ eV, $\tau = 0.15$ ps. The transverse coordinate of $(\omega - \omega_0)/\omega_{\text{gap}}$ is the normalized angular frequency, where $\omega = 2\pi c/\lambda$ is the incident angular frequency of light; $\omega_0 = 2\pi c/\lambda_0$ is the central angular frequency; arcsin represents the inverse sine function; and $\omega_{\text{gap}} = 4\omega_0\arcsin|(n_{a0} - n_{b0})/(n_{a0} + n_{b0})|^2/\pi$ is the photonic bandgap [41]. The symbol of α_T is the transmittance of light waves.
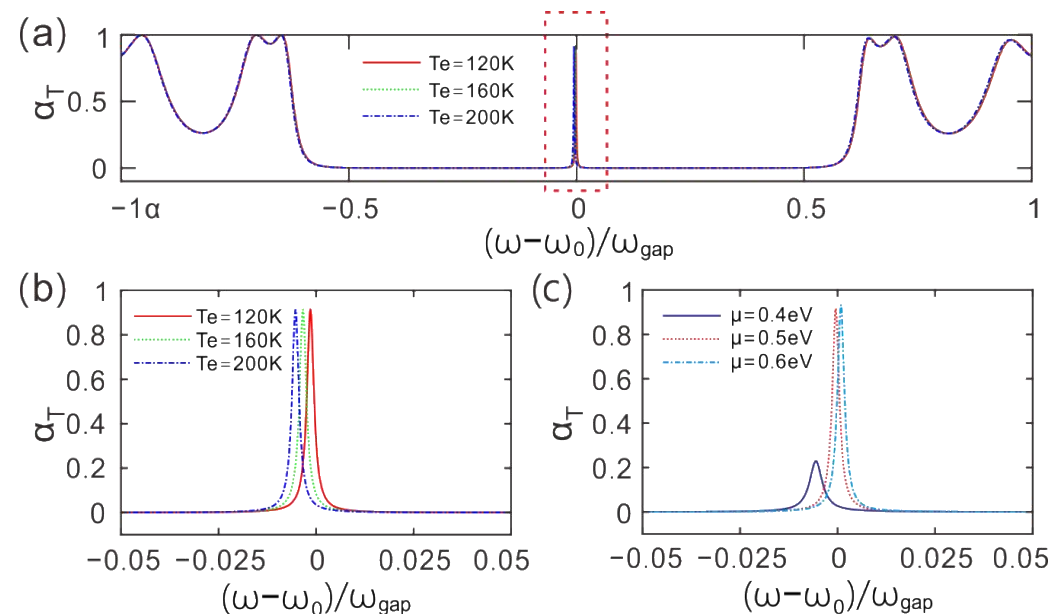

Figure 2. (**a**) Transmission spectra. (**b**) Partial enlarged view of the transmission spectra at the center of the band gap for different environment temperatures. (**c**) A local enlarged view of the transmission spectra at the center of the band gap for different graphene chemical potentials. The incidence angle is $\theta = 0°$.

Each environment temperature value corresponds to a light wave transmission spectrum curve. For $(\omega - \omega_0)/\omega_{\text{gap}} = (-1, 1)$, there is a photonic band gap in the middle of each transmission spectrum curve. In the middle of the band gap, there is a resonant transmission peak, such as the position marked by the dotted line. The central transmission mode of the band gap has a strong localization effect on the electric field. The main energy of the electric field is bound at the interface of the medium.

Figure 2b shows a local enlarged view of the transmission mode at the center of the band gap at different environment temperatures. One can see that the locations of the resonant transmission peaks corresponding to different environment temperatures are different. Obviously, the position of the resonance transmission peak moves to the left with the increase in the environment temperature value, such as the low-frequency direction. Different resonance peaks correspond to different resonance wavelengths; that is,

the central wavelength corresponding to the transmission peak wanders towards the long wavelength as the temperature increases. Therefore, the position of transmission peak, i.e., transmission wavelength, can be controlled by different environment temperatures.

Figure 2c gives a local enlarged view of the central transmission mode of the band gap for different graphene chemical potentials. The chemical potential μ can be tuned by the gate voltage V_g on graphene, and their relation can be governed by [42]

$$|\mu| = \hbar v_F \sqrt{\pi |a_0 (V_g - V_D)|}, \tag{12}$$

where the parameter $v_F \approx 10^6$ m/s is the Fermi velocity of electrons in graphene; a_0 is empirical constant and is given by $a_0 = 9 \times 10^{-16}$ m; and V_D is the offset bias voltage, and it is generally set as $V_D = 0$ for intrinsic graphene. We have added the discussion in the revised manuscript. The environment temperature is set to $T_e = 100$ K, $\tau = 0.15$ ps. It is obvious that the locations of transmission peaks corresponding to different chemical potentials are different. The position of the transmission peak moves to the left with the decrease in the chemical potential, that is, to the low frequency direction, while the central wavelength of the transmission peak changes to the long wavelength, and the peak transmittance will decrease. Therefore, the wavelength and transmittance of the central transmission mode can also be dominated by the chemical potential of graphene.

Figure 3 demonstrates the electric field distribution of the central transmission mode in the whole structure ($N = 3$). Taking $T_e = 100$ K as an example, wavelength of central resonant mode is $\lambda_p = 1.5506$ μm. The horizontal direction is the arrangement direction of the medium sheet. The ordinate represents the intensity of the component of the electric field in the horizontal direction and is normalized. One can be seen that the electric field is mainly distributed in the middle of the structure (denoted by the orange line), and the electric field intensity is the largest on the two media interfaces of AB and BA, respectively. Graphene (denoted by the red lines) is embedded on the two media interfaces between AB and BA, which have the largest electric field strength, forming a three-layer structure of AGB and BGA. The whole system structure is ABABABBGABABA. The local electric field strength at the location of graphene is the largest; the third-order nonlinear effect of graphene should be improved obviously so that the optical bistability with low threshold can be achieved.
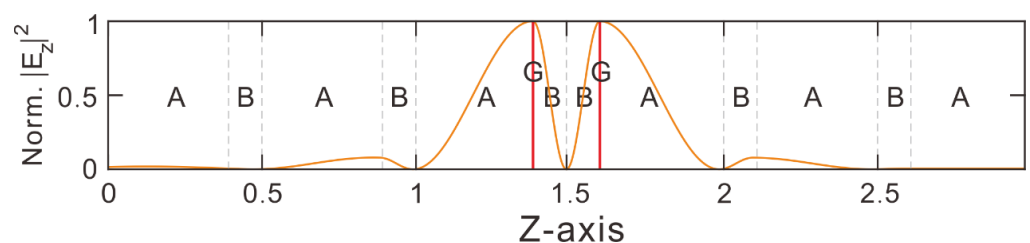

Figure 3. Distribution of electric field for the central transmission mode in transmission spectrum for light waves impinging on superconductor PCs.

The defect mode is a transmission mode in the transmission spectrum; on the other hand, it is also a localized optical mode for the longitudinal distributed field. We here give the stationary distribution of the longitudinal mode. It is similar to the mode field distribution of standing wave resonance, so the mode is static and time-free.

Figure 4a shows the input–output light intensity variation relationship under different environment temperatures for $\lambda = 1.56$ μm, which is red-detuning to that $\lambda = 1.5506$ μm in the linear spectrum. It is the condition for realizing OB. Other parameters remain unchanged. For different values of environment temperature, there are different input-output light intensity curves and in each curve; there is an S-shaped curve segment, which is the OB effect. The left and right inflection points of the S-shaped curve segment correspond to the lower threshold I_{id} and the upper threshold I_{iu} of the OB, respectively. As the value

of I_i gradually increases from a lower value to I_{iu}, the value of I_o changes upward. As the value of I_i gradually decreases from a higher value to I_{id}, the value of I_o changes downward. The upper and lower thresholds of the corresponding OB are different at different values of environment temperature. As the value of I_i changes, viz. $I_{id} < I_i < I_{iu}$, one input can correspond to two stable outputs, which is the origin of the name of OB. The above OB is further applied to the temperature control switch. The upper threshold I_{iu} corresponds to the opening threshold of the temperature control switch, and the lower threshold I_{id} corresponds to the closing threshold of the temperature control switch. The turn-on threshold and turn-off threshold are functions of the environment temperature. Therefore, the turn-on and turn-off threshold of the switch are controlled by the environment temperature.
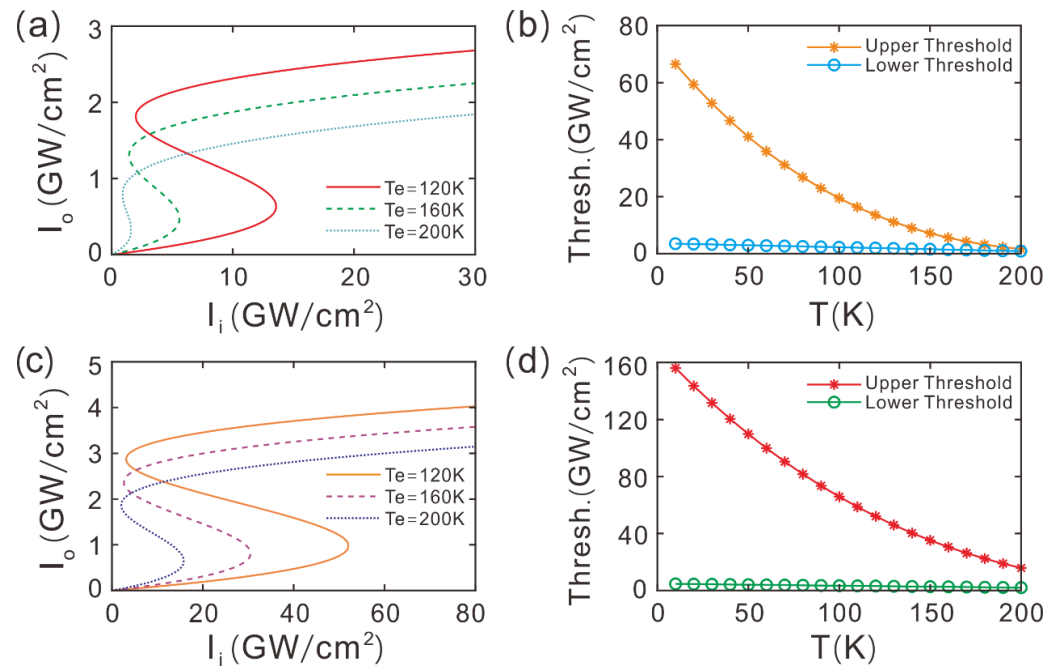

Figure 4. (**a**,**c**) The input–output light intensity variation relationship of the incidence wavelength is $\lambda = 1.56$ µm and $\lambda = 1.565$ µm, respectively. (**b**,**d**) Bistability threshold varying with the environment temperature. The incidence wavelength is $\lambda = 1.56$ µm and $\lambda = 1.565$ µm, respectively.

For a given environment temperature $T_e = 120$ K, the corresponding lower threshold and upper threshold are $I_{id} = 1.9902$ GW/cm^2 and $I_{iu} = 13.5776$ GW/cm^2, respectively. The threshold interval is $I_{int} = I_{iu} - I_{id} = 11.5874$ GW/cm^2. For $T_e = 160$ K, $I_{id} = 1.4399$ GW/cm^2 and $I_{iu} = 5.6045$ GW/cm^2. Increasing the environment temperature to 200 K, the upper threshold, lower threshold, and threshold interval are $I_{iu} = 1.6315$ GW/cm^2, $I_{id} = 0.8892$ GW/cm^2, and $I_{int} = 0.7423$ GW/cm^2, respectively. One can see that with the increase in environment temperature, the values of I_{id} and I_{iu} of the temperature control switch decrease, and the corresponding threshold interval $I_{int} = I_{iu} - I_{id}$ decreases, as shown in Figure 4b. Here, the incident wavelength is $\lambda = 1.56$ µm.

With further increasing the incident wavelength to $\lambda = 1.565$ µm, Figure 4c reveals the relationship between input intensity and output intensity of light. Other parameters remain unchanged. One can see that at different temperatures, there are still S-shaped curve segments, that is, the bistable relationship. Relative to $\lambda = 1.56$ µm, the threshold and threshold interval of the temperature control switch increase at the same environment temperature. For example, for the value of $T_e = 120$K, the upper threshold $I_{iu} = 52.0753$ GW/cm^2; the lower threshold $I_{id} = 3.1399$ GW/cm^2; and the threshold interval $I_{int} = 48.9354$ GW/cm^2. This shows that the threshold and threshold interval are affected by modulated incident wavelength.

Figure [4]d plots the threshold changing with the environment temperature for λ = 1.565 µm. It is obvious that the threshold and threshold interval of the OB decrease with the increase in environment temperature, while relative to λ = 1.55 µm, the threshold and threshold interval of the OB increase, which means that the greater the detuning of incident wavelength is, the greater it needs the threshold and threshold interval of the temperature to control switches. The larger the threshold is, the higher the light field energy is required for turning on and off. With the increase in threshold interval, the discrimination between turn-on and turn-off is more remarkable, and the misjudgment rate decreases. At the same time, we can also see that the bistable effect disappears at 0 K.

Figure [5]a provides the input–output relationship of light intensity. Here, T_e = 100 K, and λ = 1.56 µm. For the values of μ = 0.5 and 0.6 eV, we can see that there is an S-shape in each curve (i.e., an OB). For μ = 0.4 eV, there is not a S-shaped curve segment in the input–output relationship curve; i.e., the bistable relationship is not supported. However, compared with the results in the cases of μ = 0.5 and 0.6 eV, the values of I_{iu}, I_{id}, and I_{int} increase.
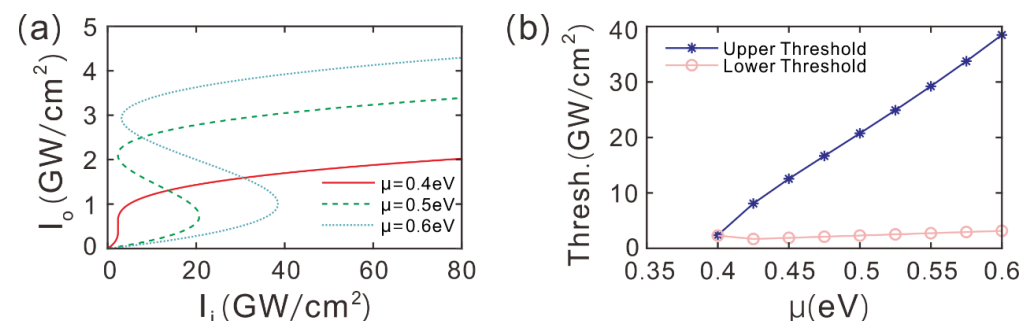

Figure 5. (**a**) Input–output light intensity relationship corresponding to different graphene chemical potentials. (**b**) Relationship between the upper and lower thresholds of bistability and the chemical potential of graphene. The incidence wavelength is λ = 1.56 µm.

Figure [5]b shows that the thresholds of OB depend on the graphene chemical potential for λ = 1.56 µm. The environment temperature is T_e = 100 K. This graph shows that the bistable action emerges as μ > 0.4 eV, the OB threshold and threshold interval increase with the increase in the graphene chemical potential. Therefore, the appearance of OB and its threshold parameters can be controlled by the chemical potential.

One can see that the nonlinear conductivity coefficient of graphene is inversely proportional to the chemical potential of graphene from Equation (7). Therefore, the nonlinearity of graphene shrinks as the increase in the potential of graphene. It needs stronger incident light energy to meet the resonant condition for a larger value of graphene chemical potential, which can be utilized to explain why the thresholds of OB increase with the increase in the chemical potential of graphene.

In our previous studies [1,3], we used the electric field localization of defect state to strengthen the nonlinear effect of graphene. The threshold parameters can be flexibly adjusted by μ, λ, and θ. Otherwise, some studies have been done on OB in PC heterostructure based on topological edge states [17,20,23]; the hysteresis behavior and OB threshold are also adjusted by the Fermi energy of graphene, as well as the wavelength and angle of the incident beam. The dielectric constant of conventional dielectrics and the conductivity of graphene are functions of temperature, but the performance of OB controlled by temperature is not obviously dependent. For our proposed project, the PC includes the following components: high-temperature superconductor and semiconductor materials. The results show that the proposed composite structure can have the same photonic band gap characteristics as the periodic structure. The dielectric constant of these materials varies with the environment temperature, which means that the threshold and threshold interval of OB can be flexibly controlled by environment temperature, rather than just through graphene and incident beam. The OB is further applied to the temperature control switch.

The upper and lower thresholds of OB correspond to the opening and closing thresholds of the temperature control switch, which is the feature of this paper.

The photonic crystal can support the defect mode as a defect is embedded at the center of the structure. The local electric field of the defect mode is the strongest in the central position, so the optical nonlinearity could be greatly enhanced under considering the three-order nonlinear effect of the defect. Optical bistability and solitons were further achieved in the defect photonic crystal [43,44]. The threshold of optical bistability can be modulated through the chemical potential of graphene which is embedded at the interfaces of the defect [45]. However, Zheng et al. neglected the nonlinearity of graphene though three-order nonlinear coefficient is an order of magnitude larger than that of the conventional dielectric, such as SiO_2 [45,46]. Otherwise, the optical soliton is a transversal distributed mode, while the defect mode is longitudinal. The optical bistability therefore results from the localization of longitudinal electric field. We here realize the optical bistability based on the nonlinearity of graphene in defect photonic crystals. Of which graphene is embedded at the site where the local electric field is the strongest in the whole system. Consequently, the nonlinearity of graphene has been greatly enhanced, and low-threshold bistability is realized.

4. Conclusions

In conclusion, the optical bistable phenomenon is investigated in one-dimensional photonic crystals composed of high-temperature superconductor, graphene, and semiconductor materials. The compound structure is symmetric to the center and approves a defect resonance mode. The central wavelength and transmittance of the defect mode change with the low environment temperature and the chemical potential of graphene. The resonant mode can greatly localize the electric field, which can be utilized to enhance the nonlinear effect of graphene. Subsequently, low-threshold optical bistability has been realized. Moreover, the thresholds values of optical bistability increase with the increase in the detuning of incident wavelength and the chemical potential of graphene. With a given value of chemical potential, fixing the incident wavelength, the bistable thresholds and thresholds interval decrease with the increase in environment temperature. The investigation may be directly applied to all-optical switches in low-temperature environment.

Data Availability Statement: Not applicable.

Conflicts of Interest: The authors declare that they have no conflict of interest.

References

1. Mao, C.; Zhong, D.; Liu, F.; Wang, L.; Zhao, D. Multiple optical bistabilities in graphene arrays-bulk dielectric composites. *Opt. Laser Technol.* **2022**, *154*, 108292. [CrossRef]
2. Kim, M.; Kim, S.; Kim, S. Optical bistability based on hyperbolic metamaterials. *Opt. Express* **2018**, *26*, 11620–11632. [CrossRef] [PubMed]
3. Zhao, D.; Wang, Z.; Long, H.; Wang, K.; Wang, B.; Lu, P. Optical bistability in defective photonic multilayers doped by graphene. *Opt. Quant. Electron.* **2017**, *49*, 163. [CrossRef]

4. Guo, J.; Jiang, L.; Jia, Y.; Dai, X.; Xiang, Y.; Fan, D. Low threshold optical bistability in one-dimensional gratings based on graphene plasmonics. *Opt. Express* **2017**, *25*, 5972–5981. [CrossRef] [PubMed]

5. Notomi, M.; Shinya, A.; Mitsugi, A.; Mitsugi, S.; Kira, G.; Kuramochi, E. Tanabe. Optical bistable switching action of Si high-Q photonic-crystal nanocavities. *Opt. Express* **2005**, *13*, 2678–2687. [CrossRef]

6. Xu, Y.; Wan, B.; Zhou, Z.; Ma, Y.; Zhang, H. Zhang. Tunable and asymmetric optical bistability of one-dimensional photonic crystals based on InSb and nonlinear materials. *Appl. Opt.* **2020**, *59*, 9799–9806. [CrossRef]

7. Litchinitser, N.M.; Gabitov, I.R.; Maimistov, A.I. Optical bistability in a nonlinear optical coupler with a negative index channel. *Phys. Rev. Lett.* **2007**, *99*, 113902. [CrossRef]

8. Lukosz, W.; Pirani, P.; Briguet, V. Optical bistability by photothermal displacement in prism coupling into planar waveguides. *Opt. Lett.* **1987**, *12*, 263–265. [CrossRef]

9. Bajoni, D.; Semenova, E.; Lemaître, A.; Bouchoule, S.; Wertz, E.; Senellart, P.; Barbay, S.; Kuszelewicz, R.; Bloch, J. Optical bistability in a GaAs-based polariton diode. *Phys. Rev. Lett.* **2008**, *101*, 266402. [CrossRef]

10. Huang, Y.; Gao, L. Tunable Fano resonances and enhanced optical bistability in composites of coated cylinders due to nonlocality. *Phys. Rev. B* **2016**, *93*, 235439. [CrossRef]

11. Xu, J.; Peng, Y.; Wang, S.; Jiang, J.; Qian, S.; Jiang, L. Optical bistability modulation based on the photonic crystal Fabry-Perot cavity with graphene. *Opt. Lett.* **2022**, *47*, 2125–2128. [CrossRef]

12. Nikitin, A.A.; Kondrashov, A.V.; Vitko, V.V.; Ryabcev, I.A.; Zaretskaya, G.A.; Cheplagin, N.A.; Konkin, D.A.; Kokolov, A.A.; Babak, L.I.; Ustinov, A.B.; et al. Carrier-induced optical bistability in the silicon micro-ring resonators under continuous wave pumping. *Opt. Commun.* **2021**, *480*, 126456. [CrossRef]

13. Zhang, K.; Gao, L. Optical bistability in graphene-wrapped dielectric nanowires. *Opt. Express* **2017**, *25*, 13747–13759. [CrossRef]

14. Zhang, H.; Virally, S.; Bao, Q.; Ping, L.; Massar, S.; Godbout, N.; Kockaert, P. Z-scan measurement of the nonlinear refractive index of graphene. *Opt. Lett.* **2012**, *37*, 001856. [CrossRef]

15. Wang, J.; Xu, F.; Liu, F.; Zhao, D. Optical bistable and multistable phenomena in aperiodic multilayer structures with graphene. *Opt. Mater.* **2021**, *119*, 111395. [CrossRef]

16. Xu, H.; Qin, Z.; Liu, F.; Zhong, D.; Liu, F. Optical bistability of graphene in PT-symmetric Thue-Morse photonic crystals. *J. Mater. Sci.* **2022**, *57*, 6524–6535. [CrossRef]

17. Peng, Y.; Xu, J.; Dong, H.; Dai, X.; Jiang, J.; Qian, S.; Jiang, L. Graphene-based low-threshold and tunable optical bistability in one-dimensional photonic crystal Fano resonance heterostructure at optical communication band. *Opt. Express* **2020**, *28*, 34948. [CrossRef]

18. Zhao, D.; Ke, S.; Hu, Y.; Wang, B.; Lu, P. Optical bistability of graphene embedded in parity-time-symmetric photonic lattices. *J. Opt. Soc. Am. B* **2019**, *36*, 1731–1737. [CrossRef]

19. Atala, M. Direct measurement of the Zak phase in topological Bloch bands. *Nat. Phys.* **2013**, *9*, 795–800. [CrossRef]

20. Long, X.; Bao, Y.; Yuan, H.; Zhang, H.; Dai, X.; Li, Z.; Jiang, L.; Xiang, Y. Low threshold optical bistability based on topological edge state in photonic crystal heterostructure with Dirac semimetal. *Opt. Express* **2022**, *30*, 20847–20858. [CrossRef]

21. Lu, L.; Joannopoulos, J.D.; Soljačić, M. Topological states in photonic systems. *Nat. Phys.* **2016**, *12*, 626–629. [CrossRef]

22. Wang, F.; Ke, S.; Qin, C.; Wang, B.; Long, H.; Wang, K.; Lu, P. Topological interface modes in graphene multilayer arrays. *Opt. Laser Technol.* **2018**, *103*, 272–278. [CrossRef]

23. Peng, Y.; Xu, J.; Wang, S.; Dong, H.; Xiang, Y.; Dai, X.; Guo, J.; Qian, S.; Jiang, L. Low-threshold and tunable optical bistability based on topological edge state in one-dimensional photonic crystal heterostructure with graphene. *IEEE Access* **2020**, *8*, 196386–196393. [CrossRef]

24. Srivastava, S.K. Study of defect modes in 1d photonic crystal structure containing high and low Tc superconductor as a defect layer. *J. Supercond. Nov. Magn.* **2014**, *27*, 101–114. [CrossRef]

25. Zamani, M. Spectral properties of all superconducting photonic crystals comprising pair of high-high, low-low or high-low temperature superconductors. *Phys. C* **2016**, *520*, 42–46. [CrossRef]

26. Sabra, W.; Elsayed, H.A.; Mehaney, A.; Aly, A.H. Numerical optimization of 1D superconductor photonic crystals pressure sensor for low temperatures applications. *Solid State Commun.* **2022**, *343*, 114671. [CrossRef]

27. Trabelsi, Y.; Ali, N.B.; Kanzari, M. Tunable narrowband optical filters using superconductor/dielectric generalized Thue-Morse photonic crystals. *Microelectron. Eng.* **2019**, *213*, 41–46. [CrossRef]

28. Liu, J.; Park, S.; Nowak, D.; Tian, M.; Wu, Y.; Long, H.; Wang, K.; Wang, B.; Lu, P. Near-field characterization of graphene plasmons by photo-induced force microscopy. *Laser Photonics Rev.* **2018**, *12*, 1800040. [CrossRef]

29. Panagopoulos, C.; Cooper, J.R.; Peacock, G.B.; Gameson, I.; Edwards, P.P.; Schmidbauer, W.; Hodby, J.W. Anisotropic magnetic penetration depth of grain-aligned $HgBa_2Ca_2Cu_3O_{8+\delta}$. *Phys. Rev. B* **1996**, *53*, R2999. [CrossRef]

30. Yamamoto, A.; Takeshita, N.; Terakura, C.; Tokura, Y. High pressure effects revisited for the cuprate superconductor family with highest critical temperature. *Nat. Commun.* **2015**, *6*, 8990. [CrossRef]

31. Samara, G. Temperature and pressure dependences of the dielectric constants of semiconductors. *Phys. Rev. B* **1983**, *27*, 3494. [CrossRef]

32. Elabsy, A. Hydrostatic pressure dependence of binding energies for donors in quantum well heterostructures. *Phys. Scr.* **1993**, *48*, 376. [CrossRef]

33. Soltani, O.; Francoeur, S.; Baraket, Z.; Kanzari, M. Tunable polychromatic filters based on semiconductor-superconductor-dielectric periodic and quasi-periodic hybrid photonic crystal. *Opt. Mater.* **2021**, *111*, 110690. [CrossRef]
34. Chen, P.Y.; Alù, A. Atomically thin surface cloak using graphene monolayers. *ACS Nano* **2011**, *5*, 5855–5863. [CrossRef]
35. Koppens, F.H.L.; Chang, D.E.; de Abajo, F.J.G. Graphene plasmonics: A platform for strong light–matter interactions. *Nano Lett.* **2011**, *11*, 3370–3377. [CrossRef]
36. Mikhailov, S.A.; Ziegler, K. Nonlinear electromagnetic response of graphene: Frequency multiplication and the self-consistent-field effects. *J. Phys. Condens. Matter* **2008**, *20*, 384204. [CrossRef]
37. Nesterov, M.L.; Bravo-Abad, J.; Nikitin, A.Y.; Garcia-Vidal, F.J.; Martin-Moreno, L. Graphene supports the propagation of subwavelength optical solitons. *Laser Photonics Rev.* **2013**, *7*, L7–L11. [CrossRef]
38. Chen, X.; Zhang, P.; Zhong, D.; Dong, J. Tunable dual- and multi-channel filter based on Cantor photonic crystals embedded with graphene. *IEEE Access* **2023**, *11*, 8433–8440. [CrossRef]
39. Sakhdari, M.; Farhat, M.; Chen, P.Y. PT-symmetric metasurfaces: Wave manipulation and sensing using singular points. *New J. Phys.* **2017**, *19*, 065002. [CrossRef]
40. Fang, Y.T.; Liang, Z.C. Unusual transmission through usual one-dimensional photonic crystal in the presence of evanescent wave. *Opt. Commun.* **2010**, *283*, 2102–2108. [CrossRef]
41. Yariv, A.; Yeh, P. *Photonic, Optical Electronic in Modern Communications*, 6th ed.; Oxford University Press: New York, NY, USA, 2007.
42. Dudek, M.; Kowerdziej, R.; Pianelli, A.; Parka, J. Graphene-based tunable hyperbolic microcavity. *Sci. Rep.* **2021**, *11*, 74. [CrossRef] [PubMed]
43. Adl, H.P.; Hajian, H.; Tajalli, P.; Tajalli, H. Optimized optical bistability in a 1D photonic crystal containing alternate layers of uniaxial anisotropic single negative materials with coupled nonlinear defects. *Optik* **2016**, *127*, 1190–1194. [CrossRef]
44. Gómez, F.R.; Mejía-Salazar, J.R. Bulk plasmon-polariton gap solitons in defective metamaterial photonic superlattices. *Opt. Lett.* **2015**, *40*, 5034–5037. [CrossRef] [PubMed]
45. Zheng, Z.; Jiang, L.; Guo, J.; Dai, X.; Xiang, Y. Tunable optical bistability in one-dimensional photonic crystal with a nonlinear defect coupled by graphene sheets. *Adv. Condens. Matter Phys.* **2017**, *2017*, 6590424. [CrossRef]
46. Ni, H.; Wang, J.; Wu, A. Optical bistability in aperiodic multilayer composed of graphene and Thue-Morse lattices. *Optik* **2021**, *242*, 167163. [CrossRef]